Research Article

One-Step Hydrothermal Synthesis of $ZnFe_2O_4$ Nano-Octahedrons as a High Capacity Anode Material for Li-ion Batteries

Zheng Xing[1], Zhicheng Ju[1] (✉), Jian Yang[2] (✉), Huayun Xu[2], and Yitai Qian[1,2]

[1] Hefei National Laboratory for Physical Sciences at Microscale and Department of Chemistry, University of Science and Technology of China, Hefei, Anhui 230026, China

[2] School of Chemistry and Chemical Engineering, Shandong University, Jinan 250100, China

© Tsinghua University Press and Springer-Verlag Berlin Heidelberg 2012

ABSTRACT

Binary transition metal oxides are considered as promising anode materials for lithium-ion batteries (LIB), because they can effectively overcome the drawbacks of simple oxides. Here, a one-step hydrothermal method is described for the synthesis of regular $ZnFe_2O_4$ octahedrons about 200 nm in size at a low temperature without further annealing being required. The $ZnFe_2O_4$ octahedrons were characterized by powder X-ray diffraction, scanning electron microscopy, high-resolution transmission electron microscopy and X-ray photoelectron spectroscopy. The electrochemical performance of the $ZnFe_2O_4$ octahedrons was examined in terms of cyclic voltammetry and discharge/charge profiles. The $ZnFe_2O_4$ octahedrons exhibit a high capacity of 910 mA·h/g at 60 mA/g between 0.01 and 3.0 V after 80 cycles. They also deliver a reversible specific capacity of 730 mA·h/g even after 300 cycles at 1000 mA/g, a much better performance than those in previous reports. A set of reactions involved in the discharge/charge processes are proposed on the basis of *ex situ* high-resolution transmission electron microscopy (HRTEM) images and selected area electron diffraction (SAED) patterns of the electrode materials. The insights obtained will be of benefit in the design of future anode materials for lithium ion batteries.

1. Introduction

Binary transition metal oxides have been considered as promising anode materials for lithium-ion batteries (LIB), because they can effectively overcome the drawbacks of simple oxides, and high specific capacity, good cycling stability and excellent rate performance can be achieved by the selection of a suitable combination of different metal oxides. So far, a variety of binary transition metal compounds have been investigated as anode materials for LIB, including M_2SnO_4 (M = Zn [1], Co [2]), MCo_2O_4 (M = Fe, Mg [3], Zn [4], and Cu [5]), MMn_2O_4 (M = Zn [6], Co and Ni [7]) and MFe_2O_4 (M = Co [8] and Ni [9]).

$ZnFe_2O_4$ stands out from the others as an anode material, due to its low toxicity, high abundance and, most importantly, high theoretical specific capacity (1072 mA·h/g). The first report of the use of $ZnFe_2O_4$ as an anode involved nanocrystalline $ZnFe_2O_4$ and Ag-doped $ZnFe_2O_4$ thin films synthesized by a pulsed laser deposition method [10]. The initial reversible capacity was 556 mA·h/g and 78% of the capacity (434 mA·h/g)

Address correspondence to Jian Yang, yangjian@sdu.edu.cn; Zhicheng Ju, juzc@ustc.edu.cn

was retained over 100 cycles. Other examples include: the reversible capacity of $ZnFe_2O_4$ nanoparticles prepared by a urea combustion method could be increased to 615 mA·h/g at a current of 60 mA/g after 50 cycles [11]; $ZnFe_2O_4$ nanofibers synthesized by an electrospinning technique delivered a reversible capacity of 733 mA·h/g after 30 cycles at 60 mA/g [12]; $ZnFe_2O_4$ hollow microspheres synthesized by a hydrothermal reaction followed by annealing at 600 °C gave a specific capacity about 900 mA·h/g over 50 cycles (with a current of 65 mA/g) [13].

Nanostructured $ZnFe_2O_4$ with specific particle shape and good crystallinity is highly desired for applications in LIB, because a small particle size can effectively shorten the reaction pathway of Li ions, increase the electron/ion conductance, and reduce the volume change induced by charge/discharge [14–16]. To date, $ZnFe_2O_4$ nanoparticles have been synthesized by the urea combustion method [11], thermal decomposition [17], hydrothermal reactions [18], sol–gel processes [19], the microemulsion method [20], and a variety of other methods [21]. Sharma et al. reported the preparation of irregular $ZnFe_2O_4$ nanoparticles by a urea combustion method that was conducted at 400 °C for 6 h and followed by annealing in air at 900 °C for 6 h [11]. Zhang and coworkers successfully fabricated porous nanocrystalline "timber-like" superstructures of $ZnFe_2O_4$ via the thermal decomposition of a zinc ferrioxalate precursor at 500 °C for 2 h [17]. Chen's group prepared $ZnFe_2O_4$ microtubes by pyrolysis of a polyvinyl alcohol (PVA)-assisted xerogel, using porous alumina as a template [22]. Peng et al. synthesized aggregated porous $ZnFe_2O_4$ nanorods by a hydrothermal reaction at 100 °C for 30 h followed by calcination at 500 °C for 2 h [18]. Porous nanorods can also be prepared by a microemulsion method followed by heat treatment at 500 °C [20]. Most of these synthetic processes require multiple reaction steps or high reaction temperature.

Herein, we have successfully developed a facile one-step hydrothermal route to prepare single crystalline $ZnFe_2O_4$ octahedrons at a low reaction temperature, using zinc acetate $(Zn(OAc)_2)$, ferrous sulfate and hydrazine hydrate as the reactants. The structure, shape and composition of the $ZnFe_2O_4$ octahedrons were investigated by X-ray powder diffraction (XRD),

scanning electron microscopy (SEM), transmission electron microscopy (TEM) and X-ray photoelectron spectroscopy (XPS). The electrochemical properties of the $ZnFe_2O_4$ octahedrons were characterized in terms of cyclic voltammetry and discharge/charge profiles. The reactions involved during the discharge/charge processes are proposed, based on the *ex situ* HRTEM analysis of the discharged and charged electrodes after 50 cycles. The well-controlled morphology and outstanding electrochemical performance of these $ZnFe_2O_4$ octahedrons will offer a good model for the exploration of the other binary oxides in the field of LIB.

2. Experimental section

All reagents (purchased from Sinopharm Chemical Reagent Co., Ltd) were analytical grade and used without further purification.

2.1 Synthesis of $ZnFe_2O_4$ Octahedrons

In a typical procedure, 0.35 g of $Zn(OAc)_2·2H_2O$ and 1 g of $FeSO_4·7H_2O$ were dissolved in 40 mL of deionized water by magnetic stirring at room temperature. Then, 5 mL of 10 mol/L $N_2H_4·H_2O$ was added into the solution. The mixture was transferred into a Teflon-lined stainless steel autoclave with a capacity about 50 mL. The autoclave was sealed, maintained at 180 °C for 14 h and cooled to room temperature. The precipitate was isolated by filtration and washed several times with distilled water and absolute ethanol. Finally, the product was dried in a vacuum oven at 60 °C for 12 h.

2.2 Characterization

XRD patterns were obtained using a Philips X'pert PRO X-ray diffractometer with Cu Kα radiation (λ = 1.541 82 Å). XPS was performed on a Thermo Scientific ESCALAB 250 X-ray photoelectronic spectrometer, using non-monochromated Mg Kα X-ray radiation as the excitation source. TEM images were taken on a Hitachi H7650 microscope. The high resolution images were recorded using a high resolution transmission electron microscope (HRTEM, JEOL-2010) operating at 200 kV. Particle morphology was characterized by a field-emission scanning electron microscope (FESEM, JEOL JSM-6700 M).

2.3 Electrochemical measurements

The electrochemical performance versus Li was measured using coin-type cells (size: 2032). To prepare the working electrodes, the active materials (60 wt.%) were mixed with Super P carbon black (30 wt.%) and polyvinylidene fluoride (PVDF) (10 wt.%) in *N*-methylpyrrolidone (NMP). After the slurry was milled (QM-3SP2 Planetary Ball Mill) for 5 hours, it was coated on a Cu foil and dried under vacuum at 80 ℃ for 12 h. The separator was a Celgard 2300 microporous membrane, and the electrolyte was a 1 mol/L solution of $LiPF_6$ in ethylene carbonate/dimethyl carbonate (EC/DMC) with a volume ratio of 1:1. The coin cells were assembled in an argon-filled glove box (Mikrouna, Super 1220/750/900) with Li metal as an anode. Galvanostatic discharge/charge tests were performed using a Land-CT2001A battery cycler (Xinnuo, Wuhan China) in the voltage range of 0.01–3.0 V (vs. Li^+/Li) at room temperature. The cyclic voltammetry (CV) profiles were recorded by a LK-2005A electrochemical workstation (Lanlike, Tianjin China).

3. Results and discussion

Figure 1 shows a typical XRD pattern of the as-prepared product. All the reflection peaks can be indexed as $ZnFe_2O_4$ in a face-centered cubic (fcc) phase (JCPDS Card Files, No. 22-1012). The strong intensity and narrow peak width indicate the good crystallinity
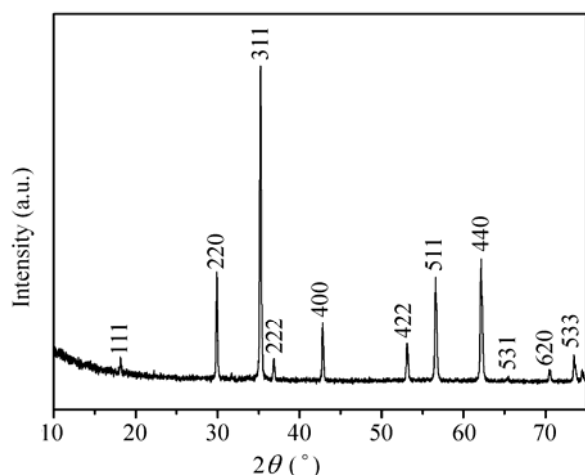

Figure 1 A typical XRD pattern of the as-prepared $ZnFe_2O_4$ octahedrons

of the product. The lattice constant calculated from the pattern is 8.453 Å, very close to the reported data (a = 8.441 Å). No peaks from any impurities are observed in the XRD pattern.

XPS was used to further confirm the formation of $ZnFe_2O_4$. As shown in Fig. 2(a), the signals of Zn, Fe and O can be identified in the product, consistent with the formation of $ZnFe_2O_4$. The presence of carbon at 284.8 eV in the spectrum can be assigned to carbon contamination, and CO_2 adsorbed on the surface of the product when it was exposed to the air after synthesis. The signals at 1045.1 and 1022.4 eV can be attributed to Zn $2p_{1/2}$ and Zn $2p_{3/2}$ of Zn^{2+} [23]. There are four signals in the high-resolution spectrum of Fe 2p, as presented in Fig. 2(c). The signals centered around 711.6 and 726.1 eV are caused by Fe^{3+} at octahedral sites. The satellite peaks, with binding energies 8 eV higher than the main peaks, confirm the oxidation state of iron is 3+ [23, 24], consistent with the reported oxidation state (Fe^{3+}) in $ZnFe_2O_4$. The O 1s peak can be found at 530.1 eV, which is characteristic of oxygen in metal oxides.

The morphology of the as-prepared $ZnFe_2O_4$ was characterized by SEM microscopy (Fig. 3). Figure 3(a) shows that the product is composed of a number of octahedrons with their sizes in the range 100–350 nm. In addition, a few vertex-truncated octahedrons were also observed. The relatively broad size distribution of the octahedrons might be caused by the overlapping of the nucleation process and the growth process, and/or Ostwald ripening due to long heating time at high temperature [25]. The magnified SEM image (Fig. 3(b)) reveals the symmetrical shape and smooth surface of the octahedrons. The regular shape of the product is in line with the fcc structure, because highly active crystal facets usually grow fast and finally vanish [26, 27]. Figure 3(c) shows a structural model of a $ZnFe_2O_4$ octahedron enclosed by eight {111} facets.

TEM microscopy offers another powerful tool to study the structure of the octahedrons. A selected area in Fig. 4(a) is used for HRTEM image and selected area electron diffraction (SAED) pattern. As shown in Fig. 4(b), the well-resolved lattice fringes suggest that the $ZnFe_2O_4$ octahedron is highly crystalline. The distances of the two different sets of crystal planes are 4.88 Å and 2.98 Å respectively, which correspond to
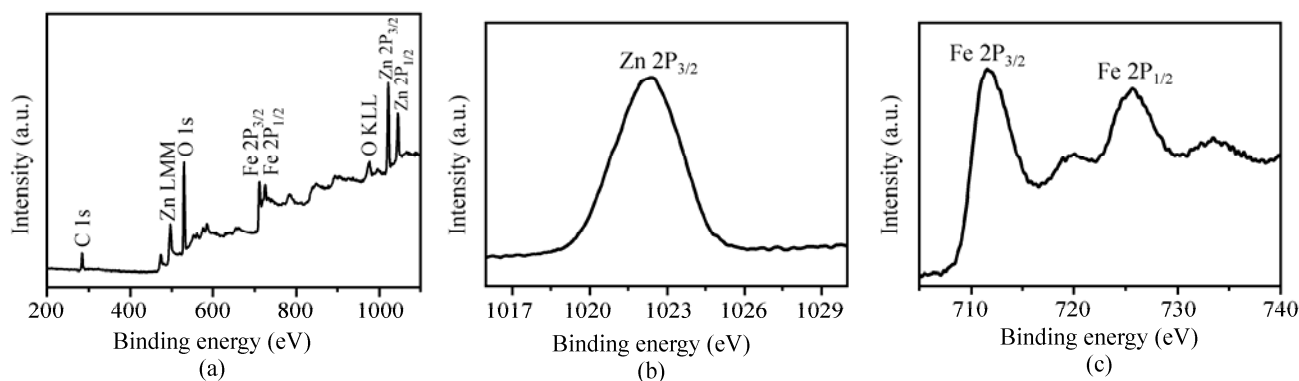
Figure 2   XPS spectra of the $ZnFe_2O_4$ samples: (a) survey spectrum; (b) Zn 2p spectrum; and (c) Fe 2p spectrum
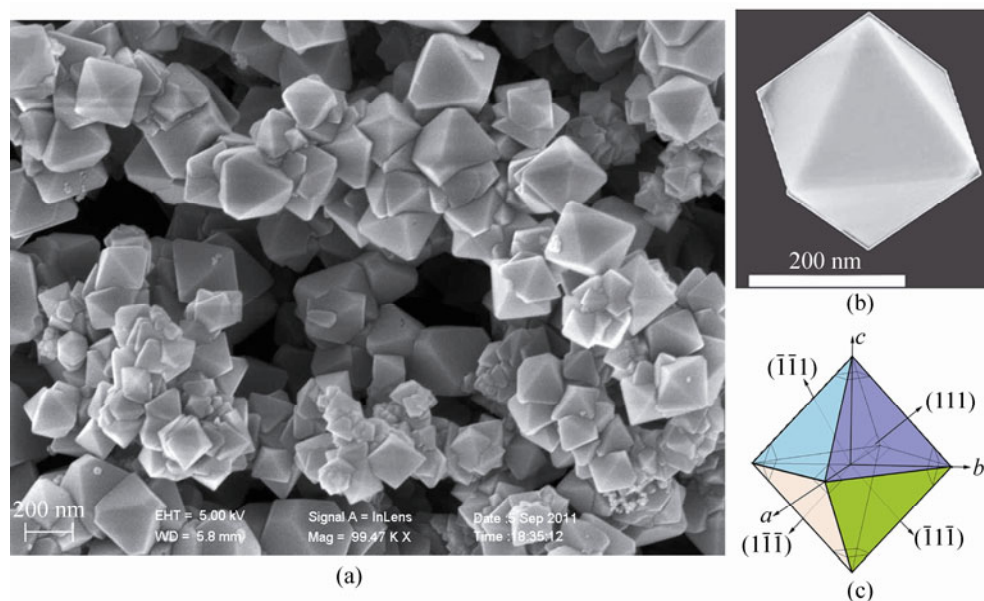

Figure 3   (a) Representative SEM image of $ZnFe_2O_4$ octahedrons; (b) SEM image of an individual $ZnFe_2O_4$ particle; (c) structure model of $ZnFe_2O_4$ octahedrons enclosed by {111} facets

the {111} and {220} crystal planes of $ZnFe_2O_4$. The fast Fourier transform (FFT) pattern of the HRTEM image (the inset of Fig. 4(b)) is in good agreement with the SAED pattern taken from the same region (Fig. 4(c)). The schematic illustration in Fig. 4(d) shows a typical crystal structure of spinel $ZnFe_2O_4$ along the $<1\bar{1}2>$ direction, the same as the HRTEM image. In this structure, O^{2-} anions are close-packed into a cubic phase. Zn^{2+} and Fe^{3+} occupy 1/8 of the tetrahedral and 1/2 of the octahedral interstitial sites in the lattice respectively.

The CV profiles for the first ten cycles at a scan rate of 0.1 mV/s are shown in Fig. 5. The cathodic peak (A) at 0.55 V in the first cycle can be assigned to the reduction reaction of $ZnFe_2O_4$ with Li into Zn^0 and Fe^0, and the further lithiation of Zn^0 to give a Li–Zn alloy [10]. Two anodic peaks (B) and (C) located at 1.57 V and 1.78 V in the first cycle might be attributed to the oxidation of Zn^0 [28] and Fe^0 [29]. During the subsequent cycles, the cathodic peak shifts to 0.93 V, which is indicative of a structure rearrangement [30, 31]. Accordingly, the anodic peaks move slightly to 1.59 V and 2.00 V.

The electrochemical performance of the sample was examined at a current rate of 60 mA/g in the potential range from 0.01 V to 3 V with Li foil as a counter electrode at room temperature (25 ℃). As presented in Fig. 6(a), the initial discharge and charge specific
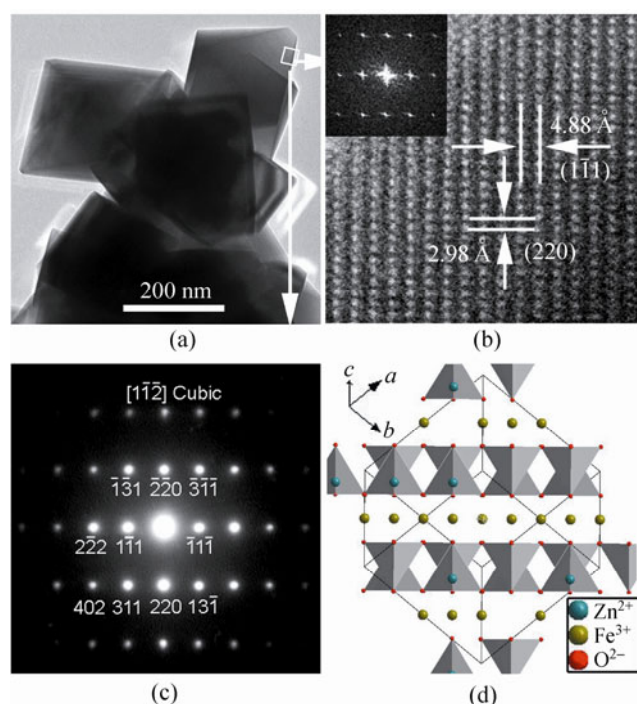
Figure 4 (a) HRTEM image of a typical $ZnFe_2O_4$ octahedron; (b) lattice fringes of the octahedron and corresponding FFT pattern (inset); (c) SAED pattern; (d) crystal structure of $ZnFe_2O_4$ crystal
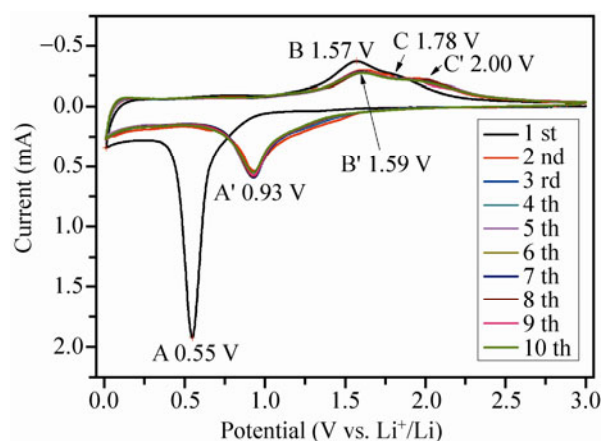

Figure 5 Cyclic voltammograms of the $ZnFe_2O_4$ electrode at a scan rate of 0.1 mV/s in the voltage range 0.01–3.0 V vs. Li^+/Li

capacities reached about 1350 mA·h/g (equivalent to ~12.1 mol Li per mol $ZnFe_2O_4$) and 1036 mA·h/g (~9.3 mol Li per mol $ZnFe_2O_4$), respectively. The extra capacity over the theoretical specific capacity might arise from the insertion of lithium ions into acetylene black [32] and interfacial storage [33, 34]. After the first cycle, the discharge plateau changed into a slope during the discharge/charge process. The change of the voltage

plateau and the significant capacity loss after the first cycle are consistent with the shifting and damping of the peaks in the CV profiles. Figure 6(b) shows the cycling performance of the $ZnFe_2O_4$/Li cell at 60 mA/g. After the third cycle, the specific capacity was stable at ~1000 mA·h/g. The discharge capacity slowly decayed but remained above 910 mA·h/g (8.15 mol Li) after 80 cycles, indicating superior capacity retention to the majority of previous reports [10–12]. As described in the Introduction, nanocrystalline $ZnFe_2O_4$ thin films only exhibited a reversible specific capacity of about 434 mA·h/g after 100 cycles [10]. This reversible capacity could be increased to 615 mA·h/g at a current density of 60 mA·h/g after 50 cycles, using $ZnFe_2O_4$ nanoparticles with a size of 100–300 nm as an anode [11]. A further increase of the reversible specific capacity to 733 mA·h/g could be achieved with $ZnFe_2O_4$ nanofibers [12]. Even after coating with carbon, $ZnFe_2O_4$ hollow spheres only delivered a specific capacity of 841 mA·h/g at 65 mA·h/g after 30 cycles [32]. The excellent performance of our $ZnFe_2O_4$ nano-octahedrons could be associated with their single-crystal nature and nanoscale size. The single-crystal nature can promote the uniform delivery of electrons and ions, and the nanoscale size can shorten Li^+ insertion/extraction pathways, increase the electron/ion conductance, and reduce the volume change caused by the charge/discharge [35, 36]. All these features enable the $ZnFe_2O_4$ nano-octahedrons to show an improved performance for LIBs. In our case, the columbic efficiency of the first cycle was about 77%. After that, the columbic efficiency between discharge and charge capacities remained above 97% from the 2nd to the 80th cycles.

The rate capacity of the $ZnFe_2O_4$ octahedrons was also studied at different current densities (Fig. 7(a)). When the current was gradually increased from 60 to 120, 240, 480 and 960 mA/g, the corresponding discharge capacities were 990, 850, 700, 640 and 575 mA·h/g respectively. If the current was reverted to 65 mA/g, the capacity returned to ~960 mA·h/g, thus almost recovering the initial capacity. Since the $ZnFe_2O_4$ octahedrons present an outstanding rate capability, the electrochemical performance at large current density (1000 mA/g) was further evaluated by two processes (Fig. 7(b)). If a high current density (1000 mA/g) was directly applied to the cell, the reversible specific
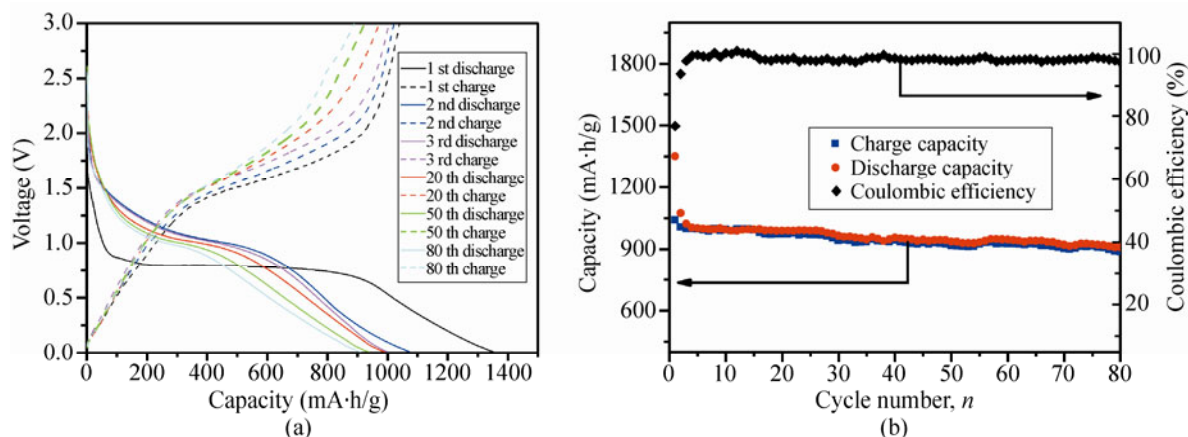
Figure 6 Electrochemical performance of the $ZnFe_2O_4$ electrode. (a) discharge/charge profiles for selected cycles; (b) discharge/charge capacity and coulombic efficiency as a function of cycle number
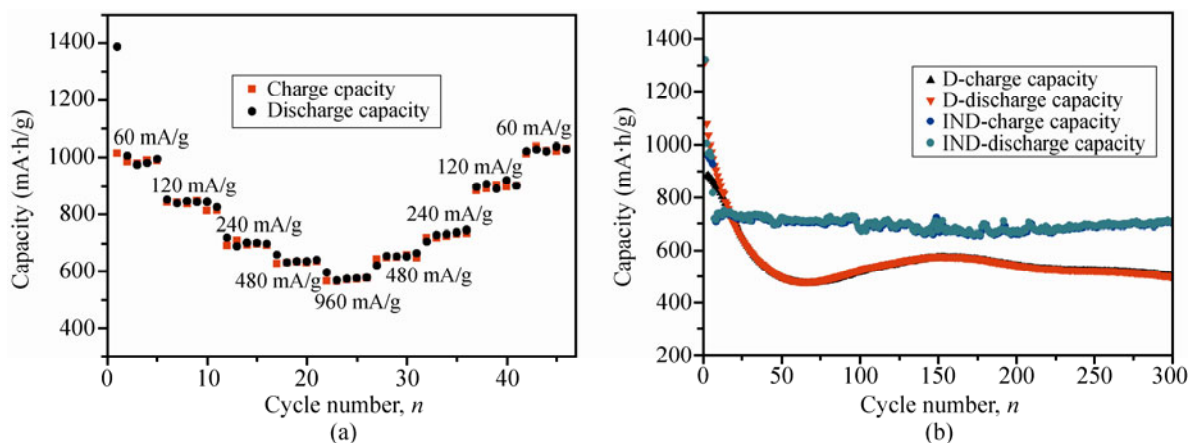

Figure 7 (a) The rate performance of $ZnFe_2O_4$ electrode (60–960 mA/g); (b) discharge/charge capacity at 1000 mA/g; the curves consisting of black and red triangles represent discharge/charge capacity when a current of 1000 mA/g was directly applied; the curves consisting of blue and green dots represent discharge/charge capacity when a current of 1000 mA/g was indirectly applied

capacity decreased rapidly to ~480 mA·h/g after 50 cycles. Then it slowly increased to ~570 mA·h/g after another 100 cycles, which might be associated with the decomposition of the electrolyte [37]. Finally, it gradually faded to ~520 mA·h/g over 300 cycles. In contrast, if the discharge/ charge current density was controlled at 60 mA/g for the first five cycles and then increased to 1000 mA/g, the reversible specific capacity could be kept at ~730 mA·h/g, much better than in all the previous reports. Using $ZnFe_2O_4$ nanofibers as an anode for LIB only delivered a specific capacity around 400 mA·h/g at 800 mA/g [12]. Similar results were observed for $ZnFe_2O_4$ hollow spheres, which exhibited a specific capacity of 500 mA·h/g at 650 mA/g [13], and $ZnFe_2O_4$/C hollow spheres that presented a specific

capacity of 450 mA·h/g at a current of 700 mA/g [32]. The capacity retention of the electrodes for 300 cycles (Fig. 7(b)) was up to 97% of that in the sixth cycle. This result indicates that directly applied high current density might induce drastic structural reorganization and result in unsatisfactory cycling performance.

Ex situ HRTEM analysis was performed on the fully discharged (0.01 V) and charged (3.0 V) electrode materials after 50 cycles to identify the lithiation and delithiation processes. As shown in Figs. 8(a) and 8(d), the initial octahedrons could not be observed after tens of discharge/charge cycles. Particles with a spheroidal morphology were found instead, indicating significant deformation and structural change. The HRTEM image (Fig. 8(b)) of the discharged electrode
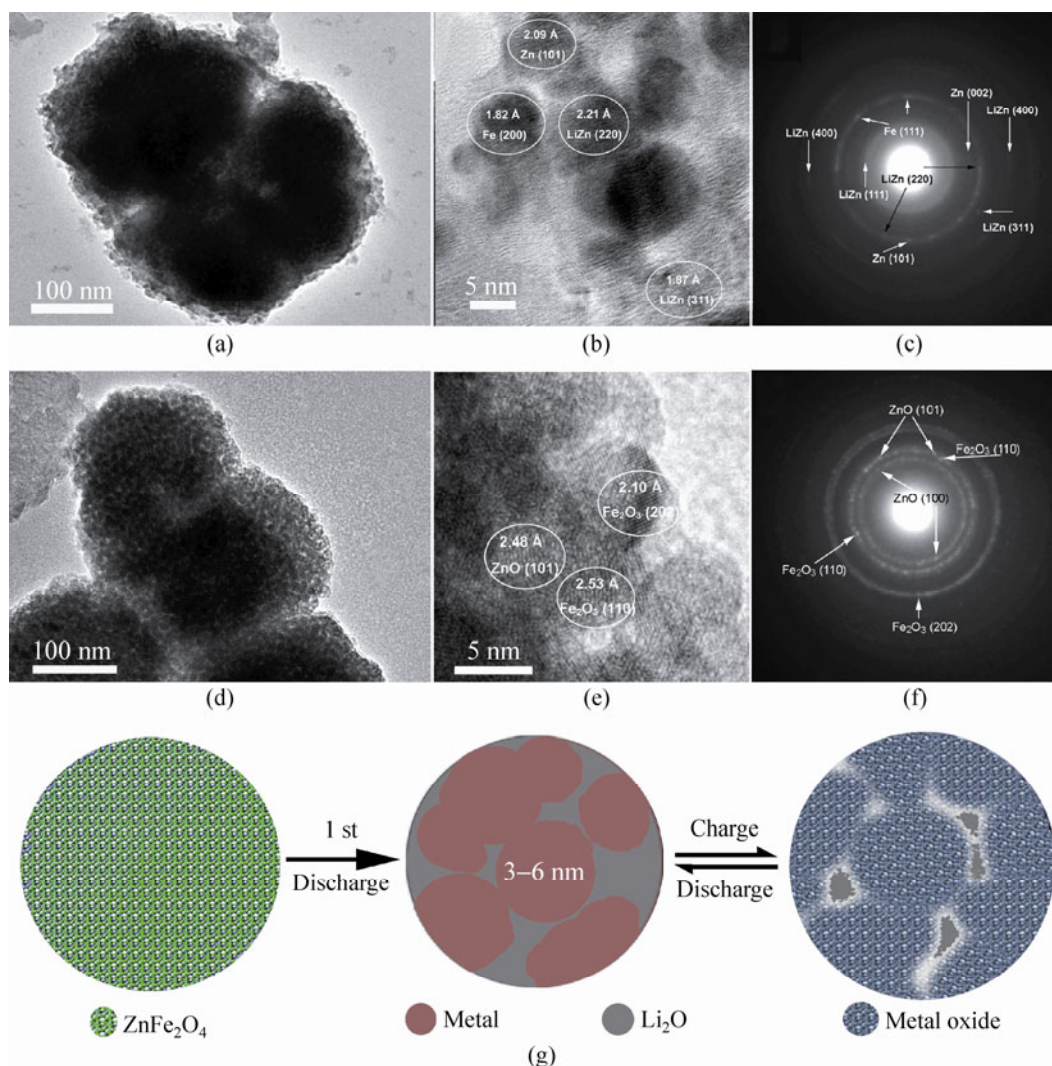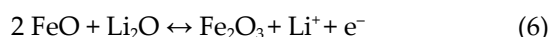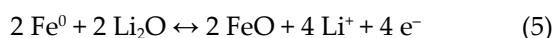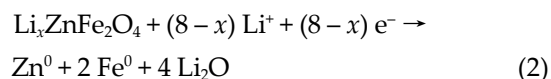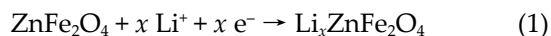
Figure 8 (a) *Ex situ* TEM image of the electrode material after being fully discharged; (b) *ex situ* HRTEM image after being discharged; (c) the corresponding SAED pattern for the material in (b); (d) *ex situ* HRTEM image after being totally recharged; (e) *ex situ* HRTEM image after being recharged; (f) the corresponding SAED pattern for the material in (d); (g) schematic illustration of the conversion reaction of $ZnFe_2O_4$ nanocrystals

shows small nanoparticles (3–6 nm) dispersed in an amorphous matrix. The lattice fringes of the crystallized particle shown in Fig. 8(b) and the corresponding diffraction rings (Fig. 8(c)) could be assigned to Zn, Fe and LiZn alloy. When the electrode was fully recharged, the lattice fringes (Fig. 8(e)) and the corresponding SAED pattern (Fig. 8(f)) confirm the presence of Fe_2O_3 and ZnO in the product, rather than $ZnFe_2O_4$.

Based on the experimental results, the following reactions are proposed to be involved in the discharge/charge cycles. During the first cycle of discharge, lithium is first intercalated into $ZnFe_2O_4$, resulting in the formation of $Li_xZnFe_2O_4$ (Eq. (1)) [11]. Then, the as-obtained $Li_xZnFe_2O_4$ is reduced by Li metal, as the discharge process continues. As a result, metallic Zn, Fe nanoparticles and amorphous Li_2O appear in the product (Eq. (2)) [37]. Finally, metallic Zn reacts with Li to form LiZn, increasing the anodic capacity (Eq. (3)). Since Eqs. (1) and (2) are irreversible, $ZnFe_2O_4$ could not be recovered in the later cycles. Metallic Zn and Fe nanoparticles can be oxidized to the respective metal oxides through the conversion reaction during the charge process, as presented in Eqs. (4)–(6) [11]. In the most favorable case, the Fe^{2+} ions in FeO would

be further reversibly oxidized to form trivalent Fe^{3+} ions to obtain Fe_2O_3 [38]. Figure 8(g) schematically outlines these changes of the $ZnFe_2O_4$ nanocrystals during discharge/charge cycles.

$$ZnFe_2O_4 + x\,Li^+ + x\,e^- \rightarrow Li_xZnFe_2O_4 \qquad (1)$$

$$Li_xZnFe_2O_4 + (8-x)\,Li^+ + (8-x)\,e^- \rightarrow$$
$$Zn^0 + 2\,Fe^0 + 4\,Li_2O \qquad (2)$$

$$Zn^0 + Li^+ + e^- \leftrightarrow LiZn \qquad (3)$$

$$Zn^0 + Li_2O \leftrightarrow ZnO + 2\,Li^+ + 2\,e^- \qquad (4)$$

$$2\,Fe^0 + 2\,Li_2O \leftrightarrow 2\,FeO + 4\,Li^+ + 4\,e^- \qquad (5)$$

$$2\,FeO + Li_2O \leftrightarrow Fe_2O_3 + Li^+ + e^- \qquad (6)$$

4. Conclusion

Spinel $ZnFe_2O_4$ octahedrons have been successfully synthesized by a facile hydrothermal route using zinc acetate and ferrous chloride as the reactants, XRD, SEM and HRTEM were used to characterize the phase, particle size and shape of $ZnFe_2O_4$. Electrochemical tests showed that the $ZnFe_2O_4$ electrode delivered an initial discharge capacity of 1350 mA·h/g at 60 mA/g. A specific capacity of 910 mA·h/g was maintained after 80 cycles. Based on the results of *ex situ* HRTEM and SAED analysis together with voltage profile and cyclic voltammetry, the reactions involved in the lithiation and delithiation processes are proposed. This material also exhibited high capacity at a high cycling rate and good cycling stability. It also delivered a large discharge specific capacity of 730 mA·h/g after 300 cycles at 1000 mA/g. This work offers a convenient method for the preparation of single crystalline $ZnFe_2O_4$ octahedrons, and a good example of their application in LIB.

Acknowledgements

References

[1] Rong, A.; Gao, X. P.; Li, G. R.; Yan, T. Y.; Zhu, H. Y.; Qu, J. Q.; Song, D. Y. Hydrothermal synthesis of Zn_2SnO_4 as anode materials for Li-ion battery. *J. Phys. Chem. B* **2006**, *110*, 14754–14760.

[2] Wang, G.; Gao, X. P.; Shen, P. W. Hydrothermal synthesis of Co_2SnO_4 nanocrystals as anode materials for Li-ion batteries. *J. Power Sources* **2009**, *192*, 719–723.

[3] Sharma, Y.; Sharma, N.; Subbarao, G.; Chowdari, B. Studies on spinel cobaltites, $FeCo_2O_4$ and $MgCo_2O_4$ as anodes for Li-ion batteries. *Solid State Ionics* **2008**, *179*, 587–597.

[4] Sharma, Y.; Sharma, N.; Subba Rao, G. V.; Chowdari, B. V. R. Nanophase $ZnCo_2O_4$ as a high performance anode material for Li-ion batteries. *Adv. Funct. Mater.* **2007**, *17*, 2855–2861.

[5] Sharma, Y.; Sharma, N.; Rao, G. V. S.; Chowdari, B. V. R. Lithium recycling behaviour of nano-phase-$CuCo_2O_4$ as anode for lithium-ion batteries. *J. Power Sources* **2007**, *173*, 495–501.

[6] Kim, S. W.; Lee, H. W.; Muralidharan, P.; Seo, D. H.; Yoon, W. S.; Kim, D. K.; Kang, K. Electrochemical performance and *ex situ* analysis of $ZnMn_2O_4$ nanowires as anode materials for lithium rechargeable batteries. *Nano Res.* **2011**, *4*, 505–510.

[7] Courtel, F. M.; Duncan, H.; Abu-Lebdeh, Y.; Davidson, I. J. High capacity anode materials for Li-ion batteries based on spinel metal oxides AMn_2O_4 (A = Co, Ni, and Zn). *J. Mater. Chem.* **2011**, *21*, 10206–10218.

[8] Li, M.; Yin, Y. X.; Li, C.; Zhang, F.; Wan, L. J.; Xu, S.; Evans, D. G. Well-dispersed bi-component-active CoO/$CoFe_2O_4$ nanocomposites with tunable performances as anode materials for lithium-ion batteries. *Chem. Commun.* **2011**, *48*, 410–412.

[9] Lavela, P.; Tirado, J. L. $CoFe_2O_4$ and $NiFe_2O_4$ synthesized by sol–gel procedures for their use as anode materials for Li ion batteries. *J. Power Sources* **2007**, *172*, 379–387.

[10] NuLi, Y. N.; Chu, Y. -Q.; Qin, Q. Z. Nanocrystalline $ZnFe_2O_4$ and Ag-doped $ZnFe_2O_4$ films used as new anode materials for Li-ion batteries. *J. Electrochem. Soc.* **2004**, *151*, A1077–1083.

[11] Sharma, Y.; Sharma, N.; Rao, G.; Chowdari, B. Li-storage and cyclability of urea combustion derived $ZnFe_2O_4$ as anode for Li-ion batteries. *Electrochim. Acta* **2008**, *53*, 2380–2385.

[12] Teh, P. F.; Sharma, Y.; Pramana, S. S.; Srinivasan, M. Nanoweb anodes composed of one-dimensional, high aspect ratio, size tunable electrospun $ZnFe_2O_4$ nanofibers for lithium ion batteries. *J. Mater. Chem.* **2011**, *21*, 14999–15008.

[13] Guo, X.; Lu, X.; Fang, X.; Mao, Y.; Wang, Z.; Chen, L.; Xu, X.; Yang, H.; Liu, Y. Lithium storage in hollow spherical $ZnFe_2O_4$ as anode materials for lithium ion batteries. *Electrochem. Commun.* **2010**, *12*, 847–850.

[14] Xiao, X. L.; Yang, L. M.; Zhao, H.; Hu, Z. B.; Li, Y. D. Facile synthesis of $LiCoO_2$ nanowires with high electrochemical performance. *Nano Res.* **2012**, *5*, 27–32.

[15] Wang, D. S.; Ma, X. L.; Wang, Y. G.; Wang, L.; Wang, Z. Y.; Zheng, W.; He, X. M.; Li, J.; Peng, Q.; Li, Y. D. Shape control of CoO and $LiCoO_2$ nanocrystals. *Nano Res.* **2010**, *3*, 1–7.

[16] Liu, C.; Li, F.; Ma, L. P.; Cheng, H. M. Advanced materials for energy storage. *Adv. Energy Mater.* **2010**, *22*, E28–E62.

[17] Wang, M.; Ai, Z.; Zhang, L. Generalized preparation of porous nanocrystalline $ZnFe_2O_4$ superstructures from zinc ferrioxalate precursor and its superparamagnetic property. *J. Phys. Chem. C* **2008**, *112*, 13163–13170.

[18] Lv, H. J.; Ma, L.; Zeng, P.; Ke, D. N.; Peng, T. Synthesis of floriated $ZnFe_2O_4$ with porous nanorod structures and its photocatalytic hydrogen production under visible light. *J. Mater. Chem.* **2010**, *20*, 3665–3672.

[19] Zhang, R.; Huang, J.; Zhao, J.; Sun, Z.; Wang, Y. Sol–gel auto-combustion synthesis of zinc ferrite for moderate temperature desulfurization. *Energ. Fuel.* **2007**, *21*, 2682–2687.

[20] Zhu, H. L.; Gu, X. Y.; Zuo, D. T.; Wang, Z. K.; Wang, N. Y.; Yao, K. H. Microemulsion-based synthesis of porous zinc ferrite nanorods and its application in a room- temperature ethanol sensor. *Nanotechnol.* **2008**, *19*, 405503.

[21] Xu, T.; Zhou, X.; Jiang, Z.; Kuang, Q.; Xie, Z.; Zheng, L. Syntheses of nano/submicrostructured metal oxides with all polar surfaces exposed via a molten salt route. *Cryst. Growth Des.* **2008**, *9*, 192–196.

[22] Zhang, G. Y.; Li, C. S.; Cheng, F. Y.; Chen, J. $ZnFe_2O_4$ tubes: Synthesis and application to gas sensors with high sensitivity and low-energy consumption. *Sensor. Actuat. B—Chem.* **2007**, *120*, 403–410.

[23] Qian, H. S.; Hu, Y.; Li, Z. Q.; Yang, X. Y.; Li, L. C.; Zhang, X. T.; Xu, R. ZnO/$ZnFe_2O_4$ Magnetic fluorescent bifunctional hollow nanospheres: Synthesis, characte-rization, and their optical/magnetic properties. *J. Phys. Chem. C* **2010**, *114*, 17455–17459.

[24] Haetge, J.; Suchomski, C.; Brezesinski, T. Ordered mesoporous MFe_2O_4 (M = Co, Cu, Mg, Ni, Zn) thin films with nanocrystalline walls, uniform 16 nm diameter pores

and high thermal stability: Template-directed synthesis and characterization of redox active trevorite. *Inorg. Chem.* **2010**, *49*, 11619–11626.

[25] Voorhees, P. W. Ostwald ripening of two-phase mixtures. *Annu. Rev. Mater. Sci.* **1992**, *22*, 197–215.

[26] Wang, Z. L. Transmission electron microscopy of shape-controlled nanocrystals and their assemblies. *J. Phys. Chem. B* **2000**, *104*, 1153–1175.

[27] Zhou, Z. Y.; Tian, N.; Li, J. T.; Broadwell, I.; Sun, S. G. Nanomaterials of high surface energy with exceptional properties in catalysis and energy storage. *Chem. Soc. Rev.* **2011**, *40*, 4167–4185.

[28] Li, H.; Huang, X.; Chen, L. Anodes based on oxide materials for lithium rechargeable batteries. *Solid State Ionics* **1999**, *123*, 189–197.

[29] Zhang, Q.; Shi, Z.; Deng, Y.; Zheng, J.; Liu, G.; Chen, G. Hollow Fe_3O_4/C spheres as superior lithium storage materials. *J. Power Sources* **2012**, *197*, 305–309.

[30] Nyten, A.; Kamali, S.; Haggstrom, L.; Gustafsson, T.; Thomas, J. O. The lithium extraction/insertion mechanism in Li_2FeSiO_4. *J. Mater. Chem.* **2006**, *16*, 2266–2272.

[31] Binotto, G.; Larcher, D.; Prakash, A. S.; Herrera Urbina, R.; Hegde, M. S.; Tarascon, J. M. Synthesis, characterization, and Li-electrochemical performance of highly porous Co_3O_4 powders. *Chem. Mater.* **2007**, *19*, 3032–3040.

[32] Deng, Y.; Zhang, Q.; Tang, S.; Zhang, L.; Deng, S.; Shi, Z.; Chen, G. One-pot synthesis of $ZnFe_2O_4$/C hollow spheres as superior anode materials for lithium ion batteries. *Chem. Commun.* **2011**, *47*, 6828–6830.

[33] Grugeon, S.; Laruelle, S.; Dupont, L.; Tarascon, J. M. An update on the reactivity of nanoparticles Co-based compounds towards Li. *Solid State Sci.* **2003**, *5*, 895–904.

[34] Balaya, P.; Li, H.; Kienle, L.; Maier, J. Fully reversible homogeneous and heterogeneous Li storage in RuO_2 with high capacity. *Adv. Funct. Mater.* **2003**, *13*, 621–625.

[35] Arico, A. S.; Bruce, P.; Scrosati, B.; Tarascon, J. M.; van Schalkwijk, W. Nanostructured materials for advanced energy conversion and storage devices. *Nat. Mater.* **2005**, *4*, 366–377.

[36] Bruce, P. G.; Scrosati, B.; Tarascon, J. M. Nanomaterials for rechargeable lithium batteries. *Angew. Chem. Int. Ed.* **2008**, *47*, 2930–2946.

[37] Poizot, P.; Laruelle, S.; Grugeon, S.; Dupont, L.; Tarascon, J. M. Nano-sized transition-metal oxides as negative-electrode materials for lithium-ion batteries. *Nature* **2000**, *407*, 496–499.

[38] Zhu, X.; Zhu, Y.; Murali, S.; Stoller, M. D.; Ruoff, R. S. Nanostructured reduced graphene oxide/Fe_2O_3 composite as a high-performance anode material for lithium ion batteries. *ACS Nano* **2011**, *5*, 3333–3338.